JOURNAL OF MATERIALS SCIENCE 30 (1995) 522–537

Long-range ordering behaviour and mechanical properties of Ni–Mo-based alloys

H. M. TAWANCY
Materials Characterization Laboratory, Metrology, Standards and Materials Division Research Institute, King Fahd University of Petroleum and Minerals, P. O. Box 1639, Dhahran 31261 Saudi Arabia

Thermal ageing for up to 1000 h at 600–800 °C was used to study the long-range ordering behaviour to Ni_4Mo and related ordered phases in selected Ni–Mo based alloys with varying Fe and Cr contents, and the corresponding effects on mechanical properties. Analytical electron microscopy and X-ray diffraction were used to characterize the microstructure. Mechanical properties were determined from microhardness and tensile tests. During the early stages of ordering, the crystallographically-related Pt_2Mo-type, DO_{22} and $D1_a$ superlattices coexisted in all alloys studied. However, depending upon the exact chemical composition, particularly the Mo, Cr and Fe contents, some of these superlattices became unstable as the ordering reaction progressed. Chromium was found to act as a stabilizer of either a Pt_2Mo-type superlattice or Ni_3Mo depending upon the Mo content; however Fe acted as a stabilizer only of Ni_3Mo. For both Cr and Fe, the tendency to stabilize Ni_3Mo was realized at relatively higher Mo contents. Ordering behaviour of commercial alloys containing minor concentrations of Cr and Fe was found to significantly vary from one heat to another depending upon the exact Mo content. Although ordering to Ni_4Mo and Ni_3Mo could lead to severe embrittlement, ordering to a Pt_2Mo-type superlattice was found to have beneficial effects on mechanical strength.

1. Introduction

Alloys based upon the Ni–Mo system such as the wrought HASTELLOY® alloys B and B-2 (HASTELLOY is a registered trademark of the Haynes International Company) have been of particular importance to the chemical process and to the petrochemical industries because of their unique combinations of environmental resistance, mechanical strength and fabrication characteristics [1, 2]. Table I summarizes their nominal chemical compositions. Alloy B-2 is essentially a low-Fe and C version of alloy B. Thermal ageing of these alloys in the temperature range of 600 to 800 °C is known to cause long-range ordering reactions resulting in the precipitation of Ni_4Mo ($D1_a$ superlattice) and/or Ni_3Mo (based upon a DO_{22} superlattice) depending upon the alloy composition [3].

Long-range ordering to Ni_4Mo and Ni_3Mo can cause severe loss of ductility leading to intergranular embrittlement [3–6]. Also, Ni_4Mo ordering was found to degrade the corrosion resistance in reducing media such as HCl [5, 6]. Most evidence points out that the embrittlement associated with Ni_4Mo ordering is related to a discontinuous ordering reaction at grain boundaries [4, 7–9], which could also have an adverse effect on corrosion resistance [5, 6]. It is typical of the brittle Ni_3Mo phase to form as long platelets leading to a considerable loss of ductility [3]. Recently, critical additions of B to Ni–Ni_4Mo alloys were found considerably to improve their room-temperature ductility [10, 11]. Also, ordering to a Pt_2Mo-type superlattice (isomorphous with Ni_2Cr) in certain Ni–Mo–Cr alloys was found to have beneficial effects on mechanical strength [6, 12–16]. Crystallographically, the Pt_2Mo-type superlattice (orthorhombic structure) is closely related to the $D1_a$ superlattice (Ni_4Mo; tetragonal structure) and DO_{22} superlattice (basis for the Ni_3Mo structure; orthorhombic) as illustrated in Fig. 1. Each superlattice can directly be derived from the parent disordered face-centered cubic (fcc) lattice

TABLE I Nominal chemical compositions of alloys B and B-2 (weight %)

Alloy	Ni	Co	Cr	Mo	Fe	Si	Mn	C	V
B	Bal.	2.5*	1.0	26–30	5*	1.0*	1.0*	0.05*	0.30
B-2	Bal.	1.0*	1.0	26–30	2.0*	1.0*	1.0*	0.02*	–

* Maximum

0022–2461

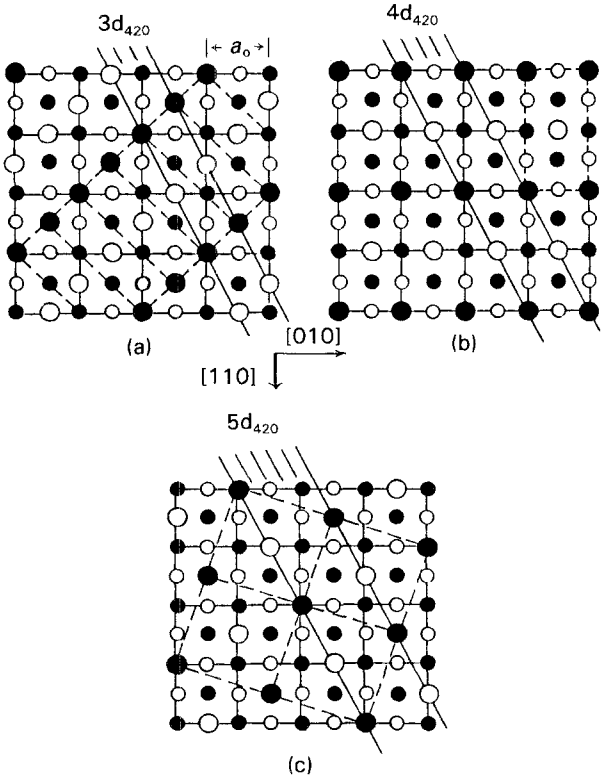

Figure 1 Atomic arrangements of various superlattices as viewed along the $[0\,0\,1]_{fcc}$ direction; unit cells are indicated by dotted lines ($a_0 \equiv$ lattice constant of the fcc crystal). Large circles, Mo atoms; small circles, Ni atoms; closed circles, atoms at level 0 or 1; open circles, atoms at level 1/2. (a) Pt_2Mo-type superlattice, (b) DO_{22} superlattice, (c) $D1_a$ superlattice.

by minor atom rearrangement on $\{4\,2\,0\}_{fcc}$ planes. In the case of the Pt_2Mo-type superlattice, each third $\{4\,2\,0\}$ plane becomes occupied with Mo atoms and planes in-between are occupied by Ni atoms (Fig. 1a) producing characteristic superlattice reflections at $1/3\langle 4\,2\,0\rangle$ positions. For the DO_{22} and $D1_a$ superlattices, the fourth and fifth planes are occupied by Mo atoms as shown in Fig. 1b and c, resulting in superlattice reflections at $1/4\langle 4\,2\,0\rangle$ and $1/5\langle 4\,2\,0\rangle$ positions, respectively.

Minor elements present in alloys of commercial grade (Table I) can have a significant effect on ordering behaviour [17, 18]. A number of studies limited to stoichiometric Ni_4Mo alloys (Ni–29.1% Mo) have dealt with the effects of Fe and Cr on the ordering behaviour [19–21]. However, it is possible that the effect of these elements is a critical function of the Mo content [13].

Toward the objective of developing ductile ordered alloys for structural applications and improving the performance of existing alloys, it is essential to develop a basic understanding of the effect of minor elements on ordering behaviour and mechanical strength. It was the objective of this study to determine the effects of selected concentrations of Fe and Cr on the ordering behaviour of Ni–Mo alloys. Also, the effect of changing the Mo content at given Fe and Cr concentrations was examined in the case of alloy B-2. For comparative purposes, the ordering behaviour of binary Ni–Mo alloys was included in the study. Emphasis was placed upon: (1) ordering kinetics; (2) nature and morphology of ordered phases; and (3) the corresponding effects on mechanical properties.

2. Experimental procedure

Four groups of alloys were included in this study: (1) three binary Ni–Mo alloys nominally containing 25% Mo, 27% Mo and 29.1% Mo (Ni_4Mo composition); (2) two heats of alloy B-2 containing the same concentrations of Fe and Cr but different Mo contents; (3) six Ni–Mo–Cr alloys containing 25% Mo, 27% Mo, 29.1% Mo and 3–5% Cr; and (4) five Ni–Mo–Fe alloys containing 27% Mo, 29.1% Mo and 2–5% Fe, all in weight percent. Tables II–V show the chemical compositions of the alloys studied. All alloys were prepared by vacuum melting and then processed into 1.5-mm-thick sheets by hot and cold rolling. Specimens were solution annealed at 1065 °C for 15 min and then water quenched. Ordering reactions were induced by thermal aging for up to 1000 h at 600, 700 and 800 °C.

Both Vickers microhardness tests and tensile tests were used to evaluate the mechanical strength. To reveal the gross grain structure, metallographic specimens were etched in a solution consisting of 80% HCl and 20% chromic acid. Bulk structural analysis was conducted on polished specimens using X-ray diffraction (CuK_α radiation). Fractography was conducted in a scanning electron microscope. An analytical electron microscope equipped with an ultra-thin window X-ray detector and operating at 200 kV was used to

TABLE II Chemical compositions of binary Ni–Mo alloys studied (weight %)

Alloy	Ni	Co	Cr	Mo	Fe	Si	Mn	C	V
1	Balance	< 0.1	< 0.1	24.96	< 0.1	< 0.02	< 0.1	0.002	–
2	Balance	< 0.1	< 0.1	26.97	< 0.1	< 0.02	< 0.1	0.002	–
3	Balance	< 0.1	< 0.1	29.06	< 0.1	< 0.02	< 0.1	0.002	–

TABLE III Chemical compositions of the heats of alloy B-2 studied (weight %)

Heat	Ni	Co	Cr	Mo	Fe	Si	Mn	C	V
A	Balance	< 0.1	0.64	26.92	0.93	< 0.02	0.24	0.002	< 0.01
B	Balance	< 0.1	0.60	28.78	0.98	< 0.02	0.25	0.002	< 0.01

TABLE IV Chemical compositions of Ni–Mo–Cr alloys studied (weight %)

Alloy	Ni	Co	Cr	Mo	Fe	Si	Mn	C	V
Hypostoichiometric alloys									
1	Balance	< 0.1	2.91	24.89	< 0.1	< 0.02	< 0.1	0.002	–
2	Balance	< 0.1	4.95	24.92	< 0.1	< 0.02	< 0.1	0.002	–
3	Balance	< 0.1	2.97	26.90	< 0.1	< 0.02	< 0.1	0.002	–
4	Balance	< 0.1	4.90	27.03	< 0.1	< 0.02	< 0.1	0.002	–
Stoichiometric alloys									
1	Balance	< 0.1	3.02	29.07	< 0.1	< 0.02	< 0.1	0.002	–
2	Balance	< 0.1	4.96	29.02	< 0.1	< 0.02	< 0.1	0.002	–

TABLE V Chemical compositions of the Ni–Mo–Fe alloys studied (weight %)

Alloy	Ni	Co	Cr	Mo	Fe	Si	Mn	C	V
Hypostoichiometric alloys									
1	Balance	< 0.1	< 0.1	26.90	2.08	< 0.02	< 0.1	0.002	–
2	Balance	< 0.1	< 0.1	27.10	2.93	< 0.02	< 0.1	0.002	–
3	Balance	< 0.1	< 0.1	26.98	4.89	< 0.02	< 0.1	0.002	–
Stoichiometric alloys									
1	Balance	< 0.1	< 0.1	29.14	2.87	< 0.02	< 0.1	0.002	–
2	Balance	< 0.1	< 0.1	29.05	4.96	< 0.02	< 0.1	0.002	–

characterize the ordered microstructure. Thin-foil specimens were prepared by a jet polishing technique in solution consisting of 30% nitric acid in methanol at about – 20 °C.

3. Results and discussion

3.1. Annealed microstructure

All alloys studied had similar grain structures in the annealed condition. Each alloy consisted of equi-axed grains about 20–70 μm in size, containing a high density of annealing twins indicating full recrystallization. In addition to characteristic face-centred cubic reflections, electron diffraction patterns derived from all alloys contained extra weak reflections at $\{1\,1/2\,0\}$ and all equivalent positions, indicating the presence of short-range order [3, 22, 23]. Examples illustrating the above structural features derived from the Ni–27 Mo alloy are given in Fig. 2.

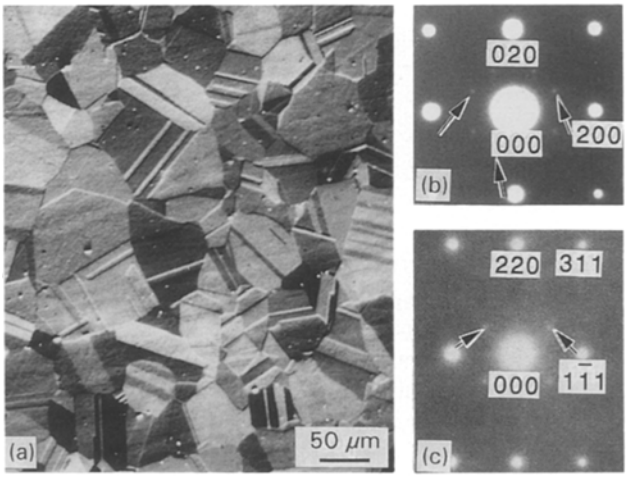

Figure 2 Characteristic microstructural features of the Ni–27 Mo alloy in the annealed condition (as-quenched). (a) Backscattered electron composition image illustrating the grain structure. (b) Selected-area diffraction pattern in [0 0 1] orientation illustrating short-range order reflections at $\{1\,1/2\,0\}$ positions (indicated by arrows). (c) Selected-area diffraction pattern in $[\bar{1}\,1\,2]$ orientation illustrating short-range order reflections at $\{1\,1/2\,0\}$ positions (indicated by arrows).

3.2. Transition from short-range to long-range order

To establish the structural transitions which occur during the early stages of ordering using electron diffraction, $\langle 0\,0\,1\rangle$ orientation was selected because it contains the short-range order reflections as well as the characteristic reflections of the Pt_2Mo-type, $D1_a$ and DO_{22} superlattices, as schematically illustrated in Fig. 3. As all the alloys studied exhibited similar structural changes during the very early stages of ordering, representative examples derived from heat A of alloy B-2 (Table III) during ageing at 700 °C are given below to illustrate the general behaviour.

Initially, the short-range order reflections present in the as-quenched condition (Fig. 2b) became connected with diffuse intensity lines along $\langle 1\,0\,0\rangle$ directions, thus passing through the $\{1\,1\,0\}$ positions characterizing the DO_{22} superlattice as shown in Fig. 4a (5 min aging at 700 °C). However, there was no specific microstructural change corresponding to this stage. With continued ageing, the diffuse intensity lines disappeared and the short-range order reflections at $\{1\,1/2\,0\}$ positions became elongated along $\langle 1\,0\,0\rangle$ directions. Simultaneously, diffuse arced intensity was found to emanate from the short-range order reflections and pass through the $1/3\langle 4\,2\,0\rangle$ positions (Pt_2Mo-type superlattice) toward the $1/5\langle 4\,2\,0\rangle$ positions ($D1_a$ superlattice) as shown in Fig. 4b (15 min ageing at 700 °C). Similar diffraction effects were predicted during long-range ordering to Ni_4Mo in binary Ni–Mo alloys based upon an Ising model of pairwise interaction [24]. Corresponding to the diffuse intensity of Fig. 4b, the microstructure exhibited a tweed

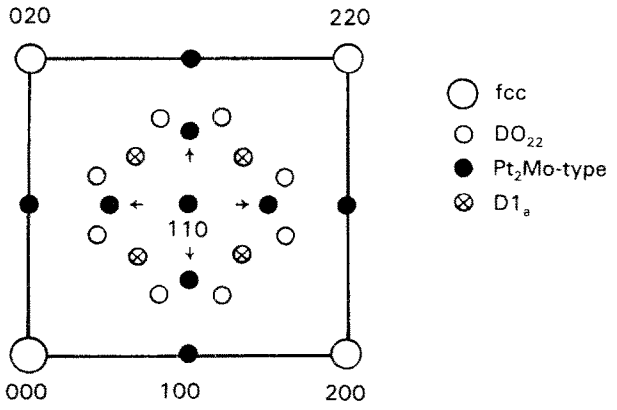

Figure 3 A schematic of the $[0\,0\,1]_{fcc}$ reciprocal-lattice intersection illustrating positions of short-range order reflections (indicated by arrows), the DO_{22} superlattice positions at $\{1\,1/2\,0\}$, $\{1\,0\,0\}$ and $\{1\,1\,0\}$, the Pt_2Mo-type superlattice positions at $1/3\langle 4\,2\,0\rangle$ or equivalently at $1/3\langle 2\,2\,0\rangle$, and the $D1_a$ superlattice positions at $1/5\langle 4\,2\,0\rangle$.

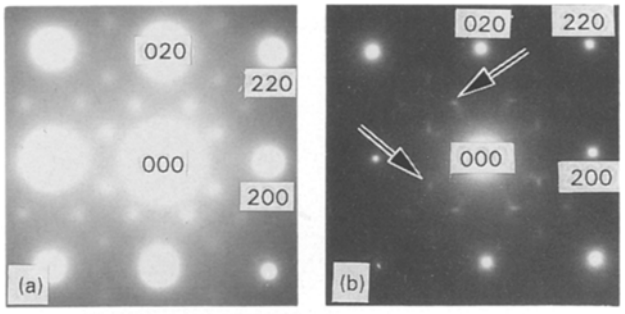

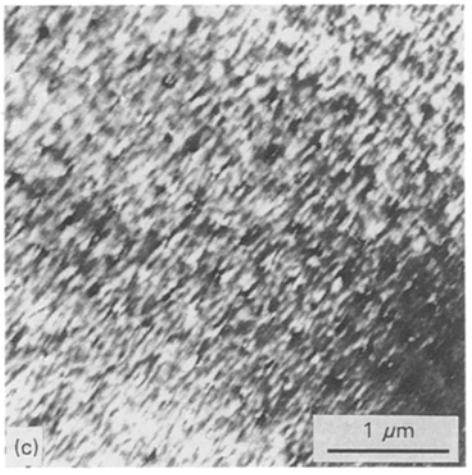

Figure 4 Representative example illustrating early stages of ordering in the alloys studied during ageing at 700 °C (Ni–26.92 Mo–0.93Fe–0.64Cr; heat A of alloy B-2 in Table III). (a) [0 0 1] selected-area diffraction pattern derived after 5 min ageing at 700 °C. (b) [0 0 1] selected-area diffraction pattern derived after 15 min of ageing at 700 °C; arrows indicate change in intensity distribution at short-range order positions. (c) Bright-field TEM image corresponding to the pattern of (b) and illustrating tweed contrast.

contrast such as that shown in Fig. 4c. Such a type of strain contrast was observed during the early stages of ordering in a number of alloy systems and could be interpreted in terms of a non-random high density distribution of strain centres in the parent disordered fcc lattice resulting from either continuous ordering or copious nucleation and growth [25].

It could be concluded from the above observations that, regardless of alloy composition, all the closely-related Pt_2Mo-type, $D1_a$ and DO_{22} superlattices (Fig. 1) had a tendency to form during the early stages of ordering, which is consistent with theoretical predictions as well as other experimental observations. According to an order–disorder theory based upon static concentration waves, it is possible that a DO_{22} superlattice could form as an intermediate transient phase during long-range ordering to Ni_4Mo and Ni_3Mo [26]. Experiments have confirmed this prediction for a number of binary Ni–Mo alloys as well as Ni–Mo alloys containing minor concentrations of Fe and Cr [27–31]. Furthermore, thermodynamic calculations based upon the first and second nearest neighbour interaction parameters for binary Ni–Mo alloys containing 16 to 25 at % Mo led to the conclusion that the ground-state structures of Pt_2Mo-type, DO_{22} and $D1_a$ superlattices have similar energies [32, 33]. As the ageing progressed at a given temperature, however, the equilibrium ordered phase(s) was found to be a function of exact chemical composition as demonstrated below.

As an example, during ageing at 700 °C, the peak of the diffuse arced intensity was transferred from the short-range order position $\{1\,1/2\,0\}$ into the $1/3\langle 4\,2\,0\rangle$ position in the case of the Ni–27 Mo–5 Cr alloy (Fig. 4b) resulting in the formation of a Pt_2Mo-type superlattice as shown in Fig. 5a. In the case of heat A

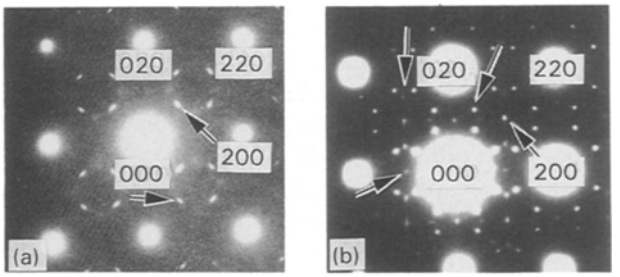

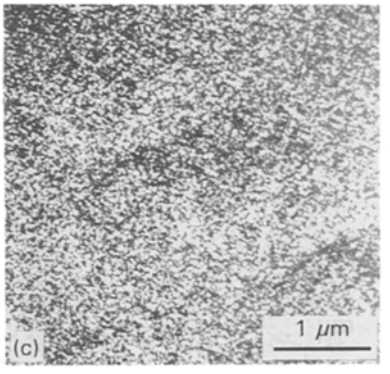

Figure 5 Representative example illustrating the development of various superlattices in the alloys studied during ageing at 700 °C. (a) [0 0 1] selected-area diffraction pattern illustrating characteristic reflections of the Pt_2Mo-type superlattice at $1/3\langle 4\,2\,0\rangle$ positions as indicated by the arrows; weak short-range order reflections can be distinguished (Ni–27 Mo–5 Cr alloy aged for 4 h at 700 °C). (b) [0 0 1] selected-area diffraction pattern illustrating the coexistence of the DO_{22} and $D1_a$ superlattices as indicated by arrows (Ni–26.92 Mo–0.93 Fe–0.64Cr; heat A of alloy B-2 in Table III).

of alloy B-2, the diffuse arced intensity was redistributed into peaks at both 1/4⟨420⟩ and 1/5⟨420⟩ positions, indicating the co-existence of the DO_{22} and $D1_a$ superlattices (Fig. 5b). Earlier studies have shown that a DO_{22} superlattice can form as an intermediate transient phase during long-range ordering to Ni_4Mo [27, 28], and both DO_{22} and Pt_2Mo-type superlattices can form during ordering to Ni_3Mo [29–31]. Dark-field images formed with any of the above superlattice reflections revealed that, at this stage of ageing, the respective ordered phase consisted of dense arrays of discrete particles as illustrated in Fig. 5c.

As indicated by the above observations, the microstructural changes which occurred during the early stages of intragranular ordering were independent of alloy composition. Initially, the microstructure contained a strain contrast characterizing either copious nucleation and growth or continuous ordering followed by the formation of dense arrays of fine ordered particles. Subsequent microstructural changes which occurred as the ordering reaction progressed with further ageing, however, were functions of the resultant ordered phase(s) depending upon alloy composition as described in the next sections.

3.3. Long-range ordering in binary Ni–Mo alloys

As expected, all the binary Ni–Mo alloys studied were ordered to Ni_4Mo after ageing at temperatures in the range of 600 to 800 °C. However, the ordering kinetics as determined from the functional dependence of microhardness and tensile properties on ageing time were accelerated with the Mo concentration. It is notable that for the stoichiometric Ni_4Mo alloy (Ni–29.1% Mo), a generalized ordering reaction occurs where diffusion of Mo over large distances is not required to establish the Ni_4Mo composition. In contrast, for the off-stoichiometric alloys where Ni_4Mo precipitates from the disordered fcc phase, diffusion of Mo over relatively large distances is required to establish the Ni_4Mo composition, and therefore the reaction kinetics become progressively slower with decreasing the Mo content [34]. Dependence of the ordering kinetics on Mo content was reflected by the changes in mechanical properties as functions of ageing time at a given temperature, as illustrated in the example given below.

Figs 6 and 7 illustrate the effect of ageing time at 700 °C on the room-temperature microhardness and the tensile properties of the binary alloys studied, respectively. For the Ni–29.1% Mo both the hardness and yield strength reached their maximum values within the first 15 min of ageing and then remained essentially unchanged with continued ageing. However, for the Ni–27Mo alloy, the hardness and yield strength reached their maximum value within the first hour of ageing. In contrast, both the hardness and tensile properties of the Ni–25% Mo alloy remained unchanged relative to the annealed condition after 24 h of ageing, reflecting the comparatively sluggish ordering kinetics as further confirmed by microstructural characterization.

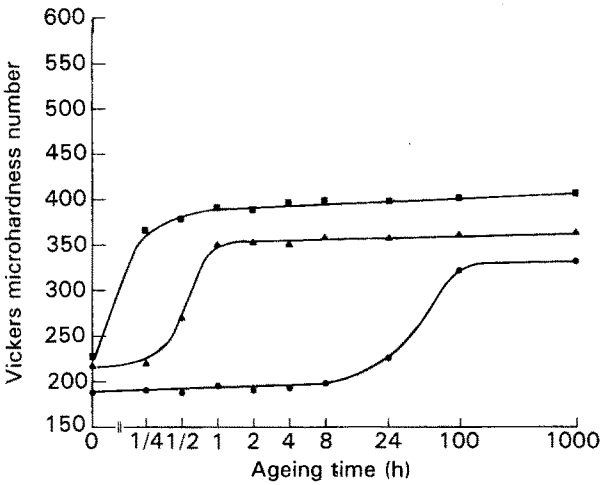

Figure 6 Effect of ageing time at 700 °C on the room-temperature microhardness of the binary Ni–Mo alloys studied. ●, Ni–25Mo; ▲, Ni–27Mo; ■, Ni–29.1Mo.

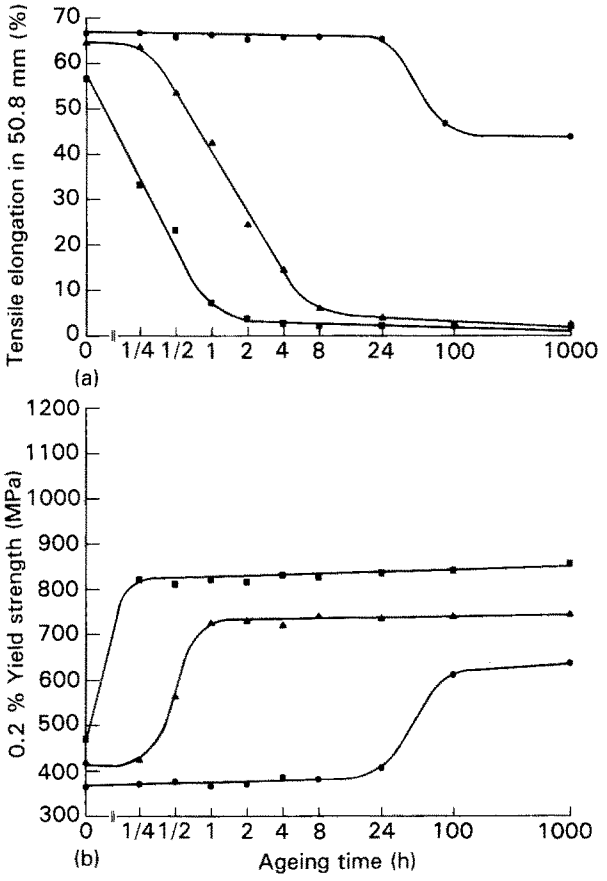

Figure 7 Effect of ageing time at 700 °C on the room-temperature tensile properties of the binary Ni–Mo alloys studied. (a) Elongation; (b) 0.2% yield strength. ●, Ni–25Mo; ▲, Ni–27Mo; ■, Ni–29.1Mo.

As can be seen from Fig. 7, the Ni–29.1% Mo alloy differed from the Ni–27% Mo alloy in that there was a one-to-one correspondence between the increase in strength and decrease in ductility. In the case of the Ni–27 Mo alloy, the decrease in tensile ductility lagged behind the increase in strength. Such a difference in behaviour could be correlated with the occurrence of a discontinuous grain boundary ordering reaction, and the dependence of its kinetics on the Mo concentration, as described below.

Intragranular ordering to Ni_4Mo is known to result in a mosaic assembly of twin-related variants along the $\{1\,0\,0\}_{fcc}$ planes [3]. With continued ageing, the dense arrays of ordered particles observed in the early stages (Fig. 5c) grew to impingement, resulting in an assembly of twin-related variants lined up along $\{1\,0\,0\}_{fcc}$ planes as illustrated in Fig. 8. As a result of further ageing, the twin-related variants were considerably coarsened as can be seen by comparing Figs 8 and 9.

Comparative microstructures representing different growth stages of Ni_4Mo in the alloys studied after ageing at 700 °C are shown in Fig. 10. After 24 h of ageing, the twin-related variants were well developed in the Ni–29.1% Mo and Ni–27% Mo alloys, as shown in Fig. 10a and b, respectively. However, the structure of the Ni–29.1% Mo alloy was coarser in comparison with that of the Ni–27% Mo alloy. For the Ni–25% Mo alloy there was no evidence for the presence of Ni_4Mo after 24 h of ageing. However, after

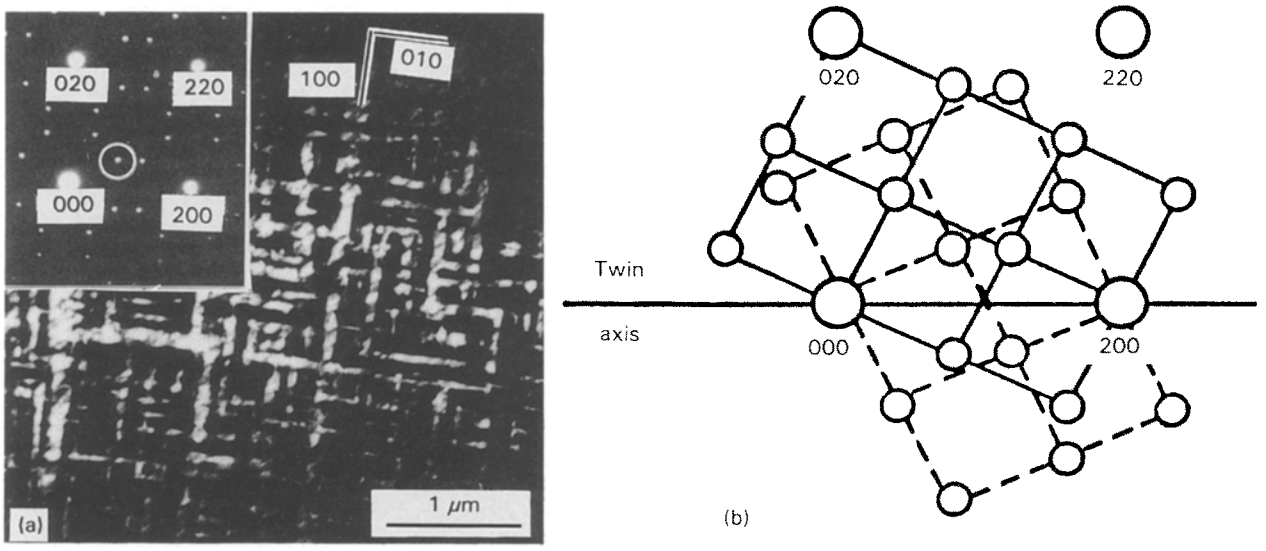

Figure 8 Example illustrating the twin relationship between Ni_4Mo crystals across $\{1\,0\,0\}_{fcc}$ planes (Ni–27 Mo alloy aged for 24 h at 700 °C). (a) Dark-field TEM image formed with the encircled Ni_4Mo reflection in the [0 0 1] diffraction pattern of the inset. (b) Interpretation of the pattern in (a) as two twin-related patterns along $\langle 1\,0\,0\rangle_{fcc}$ direction.

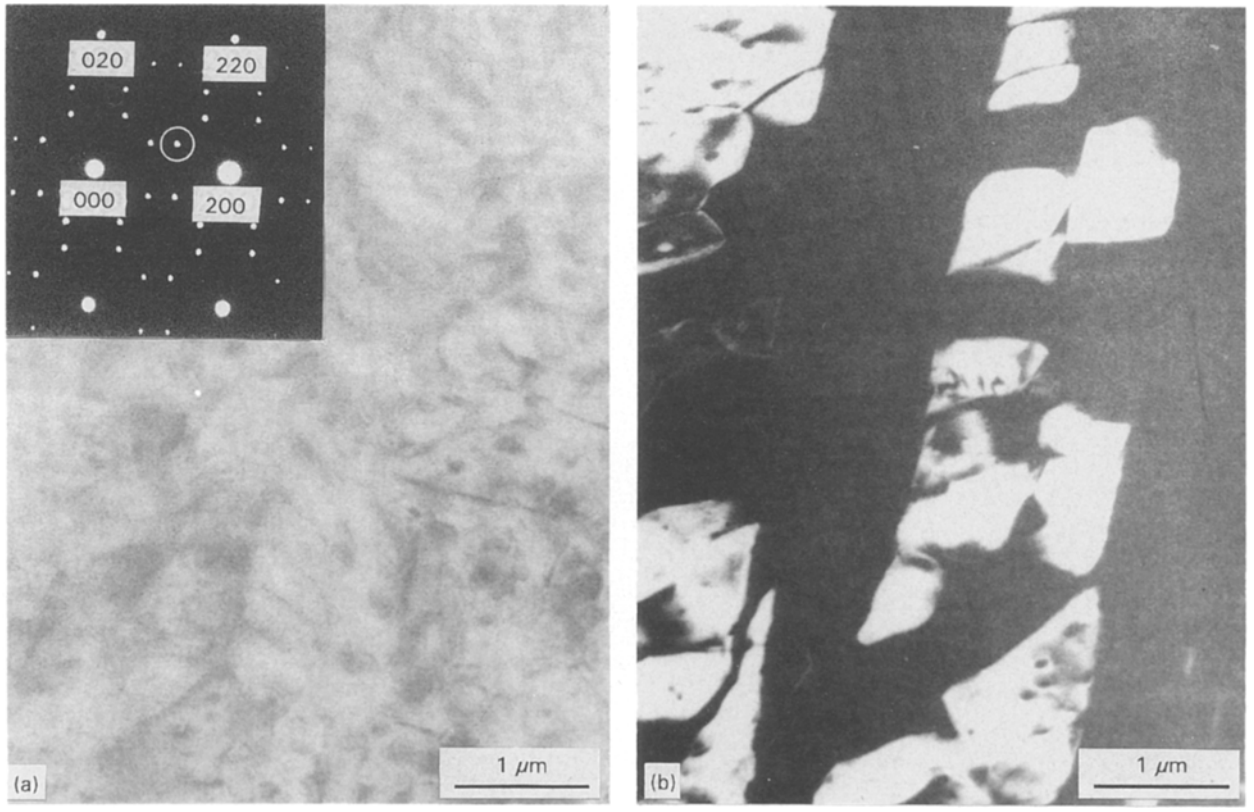

Figure 9 A typical microstructure of the Ni–27Mo alloy after 1000 h of ageing at 700 °C. (a) Bright-field TEM image; characteristic reflections of the $D1_a$ superlattice of Ni_4Mo are observed in the corresponding [0 0 1] diffraction pattern shown in the inset. (b) Dark-field TEM image formed with the encircled $1/5\langle 4\,2\,0\rangle$ superlattice reflection in (a).

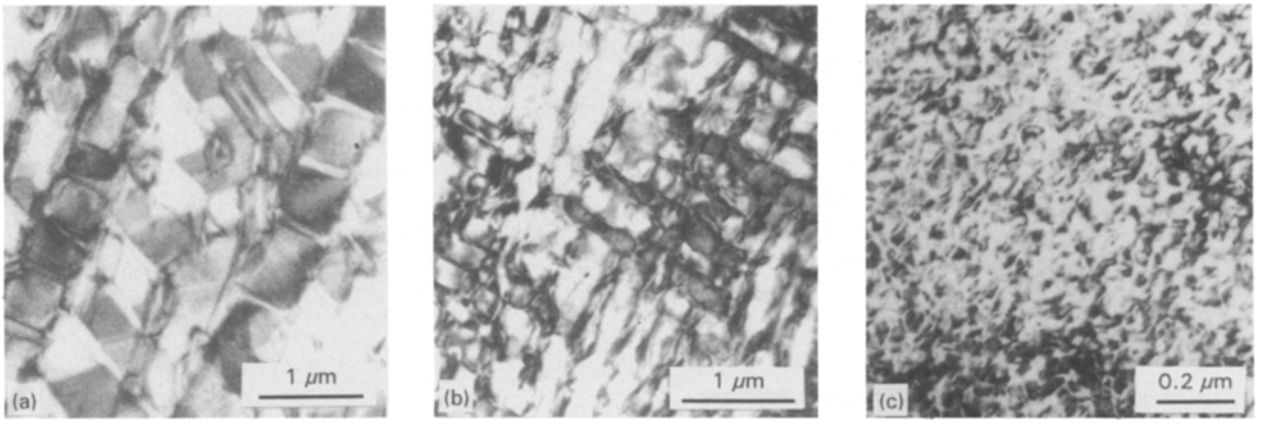

Figure 10 Bright-field TEM images illustrating the microstructure of Ni_4Mo in the binary Ni–Mo alloys aged at 700 °C. (a) Ni–29.1 Mo alloy aged for 24 h at 700 °C; (b) Ni–27 Mo alloy aged 24 h at 700 °C; (c) Ni–25Mo alloy aged 100 h at 700° C.

100 h of ageing, the alloy exhibited a strain contrast characteristic of a large volume fraction of coherent fine particles as shown in Fig. 10c, consistent with the sluggishness of the ordering reaction in this alloy as described above.

During the later stages of ageing, a lamellar structure of Ni_4Mo was observed at grain boundaries, as shown in the example of Fig. 11 (Ni–27 Mo alloy aged for 100 h at 700 °C) indicating a discontinuous grain boundary reaction. Earlier studies have shown that the matrix strain energy associated with intragranular ordering could be minimized by self-generated or strain-induced recrystallization, resulting in a discontinuous ordering reaction at grain boundaries [25, 35] such as that shown in Fig. 11. A lamellar grain boundary structure similar to that shown in Fig. 11 was observed in the stoichiometric Ni–29.1% Mo alloy earlier during ageing at 700 °C, indicating greater reaction kinetics in comparison with the Ni–27% Mo alloy. This could be explained in terms of differences in matrix strain energy between the two alloys after a given ageing time. Generally, matrix strain energy can act in certain alloy systems as the driving force for a discontinuous grain boundary precipitation reaction [36]. In the present case, increasing the Mo concentration would be expected to accelerate the kinetics of intragranular ordering and increase the associated matrix strain energy, resulting in a greater driving force for the grain boundary reaction. As the order-induced embrittlement was correlated with the discontinuous reaction [4, 7–9], the above argument could explain the lag between the increase in strength, which is primarily associated with intragranular ordering, and decrease in ductility observed in off-stoichiometric alloys (Fig. 7).

3.4. Ordering behaviour of alloy B-2

As determined from the effect of ageing time at various temperatures on the room-temperature microhardness and tensile properties, the ordering kinetics of alloy B-2 were found to be somewhat slower in comparison with a binary Ni–Mo alloy containing the same Mo content. For example, Fig. 12 illustrates the effect of aging time at 700 °C on the room-temperature microhardness of heat A in Table III, nominally containing 27% Mo and the binary Ni–27% Mo alloy. As can be seen, the hardening rate of the binary alloy was higher in comparison with the heat of alloy B-2, particularly during the early stages of ageing. Possibly, minor elements present in alloy B-2 could reduce the diffusivity of Mo in Ni, leading to slower ordering kinetics. Also, as demonstrated below, those elements were found to have significant effects on the nature of ordered phase(s) depending upon the Mo content.

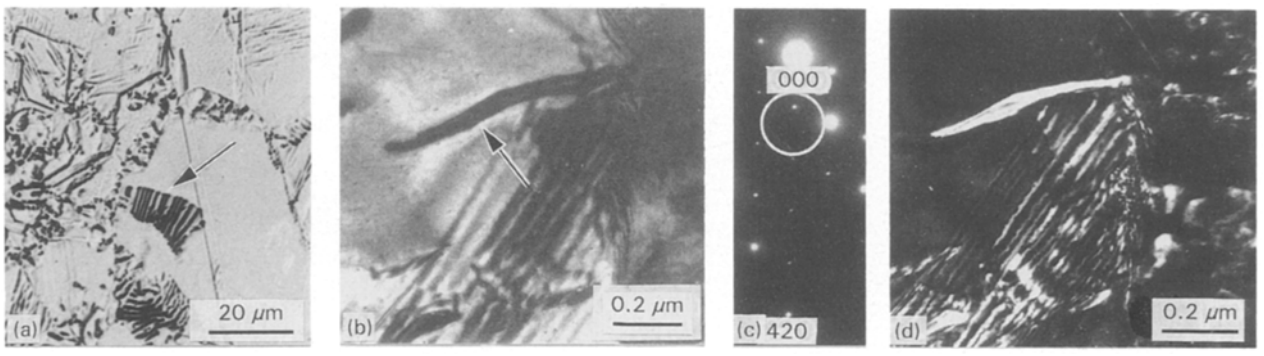

Figure 11 An example illustrating discontinuous grain boundary precipitation of Ni_4Mo in the Ni–27Mo alloy after ageing for 100 h at 700 °C. (a) Light optical micrograph illustrating lamellar structure at grain boundaries. (b) Bright-field TEM image of a grain boundary lamella. (c) Corresponding selected-area diffraction pattern illustrating characteristic superlattice reflections of Ni_4Mo at $1/5\langle 420\rangle$ positions.

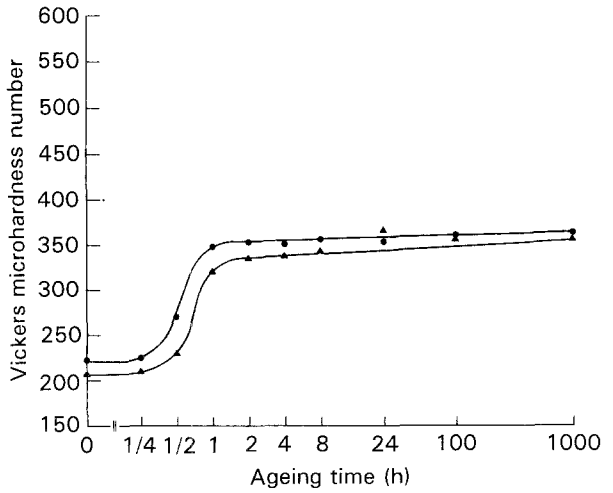

Figure 12 Comparative effect of ageing time at 700 °C on the room-temperature microhardness of the Ni–27Mo alloy and heat A of alloy B-2. ●, Ni–27Mo alloy; ▲, alloy B-2 (heat A in Table III).

Fig. 13 summarizes the effect of up to 1000 h of ageing at 600, 700 and 800 °C on the room-temperature tensile properties of the two heats of alloy B-2 studied. Reference to Table III indicates that both heats had essentially the same concentrations of Fe, Cr, Mn and Si. However, the Mo content of heat B (28.78Mo) was greater than that of heat A (26.92Mo) by about 2%. After a given ageing time at 600 °C up to 100 h, both heats had about the same yield strength and tensile ductility. Although after 1000 h of exposure, both heats continued to have the same yield strength, heat A (26.92Mo) suffered a complete loss of ductility while heat B (28.78Mo) maintained about 60% of its initial tensile ductility. Both heats behaved in a similar fashion over the entire ageing period at 700 °C, although heat A (26.92Mo) continued to lose tensile ductility at a somewhat faster rate in comparison with heat B (28.78% Mo). As can be seen from Fig. 13, the behaviour observed at 600 °C was reversed as the temperature was raised to 800 °C. After up to 24 h of ageing at 800 °C, both heats can be seen to have about the same tensile ductility. Corresponding to this condition, X-ray diffraction data showed that both heats remained to consist of fcc solid solution. However, further aging caused heat B (28.78Mo) to lose tensile ductility at a considerably faster rate in comparison with heat A (26.92 Mo). After 1000 h of exposure at 800 °C, heat A (26.92Mo) maintained about 55% of its initial tensile ductility; however heat B (28.78Mo) suffered a complete loss of ductility. It is evident from the above observations that the ordering behaviour of alloy B-2 is a sensitive function of exact chemical composition and ageing temperature, as further demonstrated below.

Using both X-ray diffraction and electron diffraction, Ni_4Mo was the only ordered phase identified in heat A (26.92Mo) after 100–1000 h of exposure at 600, 700 and 800 °C, indicating that the behaviour of this heat was similar to that of a binary Ni–Mo alloy. A lamellar structure of Ni_4Mo at grain boundaries similar to that shown in Fig. 11 was observed only after 1000 h of exposure at 600 °C, explaining the corresponding severe loss of ductility. However, this structure was well developed during the earlier stages of ageing at 700 °C, which could be related to the increased matrix strain energy associated with comparatively faster kinetics of intragranular ordering. As the temperature was raised to 800 °C, the volume fraction of Ni_4Mo was considerably reduced as would be expected, and there was no evidence for the occurrence of the grain boundary reaction explaining the observed moderate loss of ductility.

In contrast with the behaviour of heat A (26.92Mo) described above, after 1000 h of exposure at 600 °C, both Ni_4Mo and a DO_{22} superlattice (basis for the Ni_3Mo structure) were identified in heat B (28.78 Mo) as shown in the $\langle 0\,0\,1 \rangle$ electron diffraction pattern of Fig. 14a. Dark-field imaging of Ni_4Mo reflections revealed dense arrays of discrete particles as shown in Fig. 14b. Streaking of the characteristic DO_{22} superlattice reflections along $\langle 0\,0\,1 \rangle$ directions (Fig. 14a) could be interpreted in terms of the platelet morphology shown in Fig. 14c. It is well known that the DO_{22} superlattice forms on the $\{0\,0\,1\}$ planes of the parent disordered fcc lattice in other alloy systems [37–39]. Over the entire ageing time at 600 °C, there was no evidence for discontinuous grain boundary precipitation of Ni_4Mo, unlike the case of heat A (26.92 Mo), which could be related to the restricted growth of the ordered domains (Fig. 14). This could explain the observation that heat B (28.78 Mo) maintained a high ductility level. However, after 1000 h of ageing at 700 °C, Ni_4Mo was the only ordered phase identified in heat B (28.78 Mo) similar to the case of heat A (26.92 Mo), suggesting the possibility that the DO_{22} superlattice observed at 600 °C was present as an intermediate transient phase during ordering to Ni_4Mo as pointed out earlier. After 1000 h of ageing at 800 °C, the only ordered phase identified in heat B (27.78 Mo) was Ni_3Mo as shown in the example of Fig. 15, explaining the observed severe loss of tensile ductility. It is also evident from this observation that the ordering behaviour of heat B (28.78 Mo) was a function of ageing temperature unlike the case of heat A (26.92 Mo). As can be seen from Fig. 15a, Ni_3Mo assumed the morphology of long thin platelets. Corresponding electron diffraction patterns in $[0\,0\,1]_{fcc}$ and $[1\,1\,1]_{fcc}$ orientations are shown in Fig. 15b and c, respectively. Similar to a DO_{22} superlattice, the orthorhombic structure of Ni_3Mo has three twin-related variants producing superlattice reflections at $\{1\,0\,0\}$, $\{1\,1/2\,0\}$ and $\{1\,1\,0\}$ positions of the parent fcc reciprocal lattice [3]. An energy dispersive X-ray spectrum representative of Ni_3Mo is shown in Fig. 15d, and the results of quantifying the spectral data using the thin-film approximation [40] are given in Fig. 14e in comparison with the matrix composition (fcc solid solution). Relative to the matrix, Ni_3Mo was enriched in both Fe and Cr, suggesting that both elements had stabilized Ni_3Mo in heat B (27.78Mo).

Based upon the above results, the presence of minor concentrations of Cr and Fe in alloy B-2 could have a significant effect on its ordering behaviour. However, for given Cr and Fe contents, this effect appears to be a function of the exact Mo content. Toward the lower

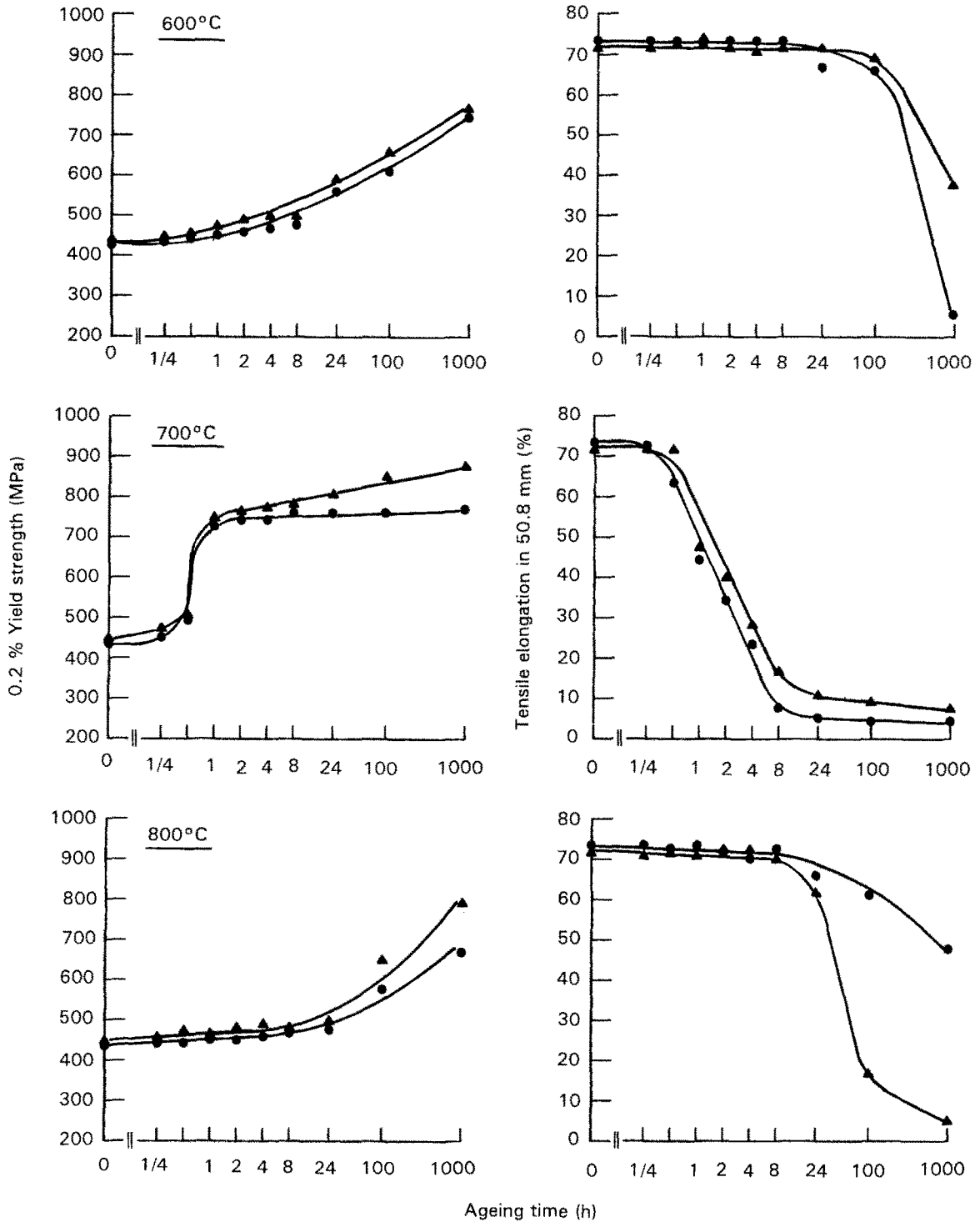

Figure 13 Room-temperature tensile properties of heats ●, A and ▲, B of alloy B-2 (Table III) as functions of ageing time at 600, 700 and 800 °C.

limit of Mo specification (Table I), the results indicated that the ordering behaviour approaches that of a binary Ni–Mo alloy containing the same Mo content. However, a considerable deviation from binary behaviour is realized as the upper limit of Mo is approached, leading to variations in ordering behaviour from one heat to another. Evidently, minor concentrations of Cr and Fe could stabilize Ni_3Mo as the upper limit of Mo is approached.

3.5. Effect of Cr on ordering behaviour

For a given Cr concentration within the range studied (up to 5%), the ordering behaviour was found to be a function of the Mo content. In alloys containing 25–27% Mo and 3–5% Cr, the predominant ordered phase was found to have a Pt_2Mo-type superlattice. However, increasing the Mo content to 29.1% at the same Cr level was found to promote the formation of Ni_3Mo.

To demonstrate the effect of Cr on the ordering behaviour, Fig. 16 illustrates the effect of up to 1000 h of ageing at 700 °C on the room-temperature tensile properties of the Ni–27 Mo and Ni–27 Mo–5Cr alloys. Relative to the annealed condition, the 0.2% yield strength of both alloys increased by about 80–85% after the ageing. Although the Ni–27 Mo alloy suffered an almost complete loss of ductility after 24 h of

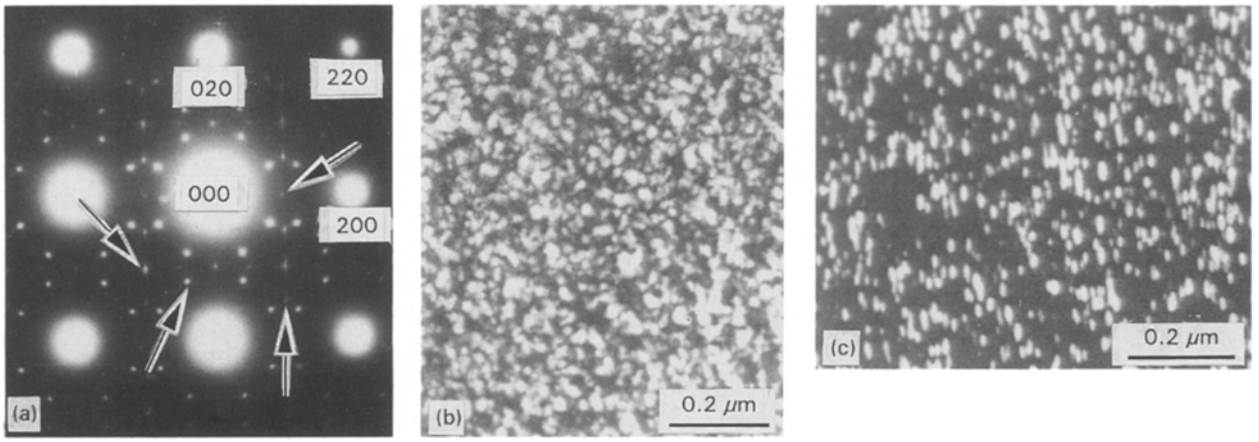

Figure 14 An example illustrating the coexistence of $D1_a$ and DO_{22} superlattices in alloy B-2 after 1000 h of ageing at 600 °C (heat B:Ni–28.78Mo–0.98Fe–0.60Cr). (a) [0 0 1] selected-area diffraction pattern illustrating $D1_a$ and DO_{22} superlattice reflections at $1/5\langle 4\,2\,0\rangle_{fcc}$ and $1/4\langle 4\,2\,0\rangle_{fcc}$ positions, respectively, as indicated by the arrows. (b) Dark-field TEM image formed with a $D1_a$ superlattice reflection. (c) Dark-field TEM image formed with DO_{22} superlattice reflection.

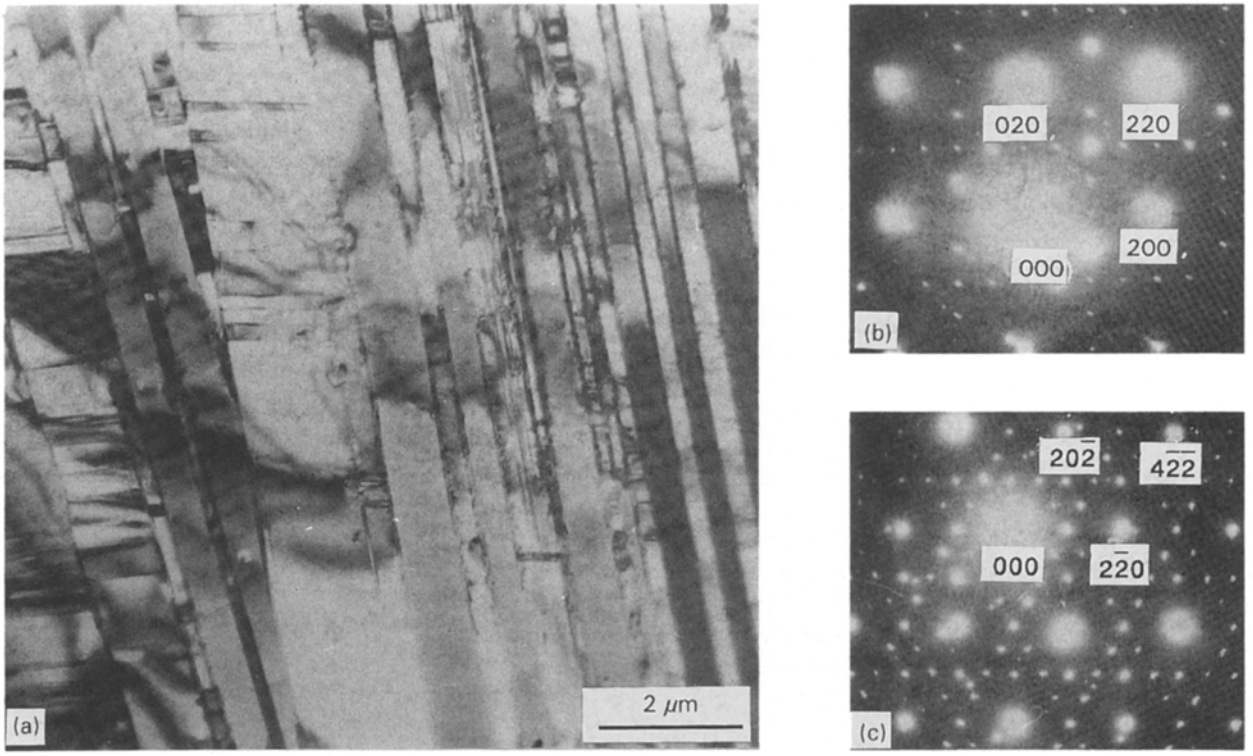

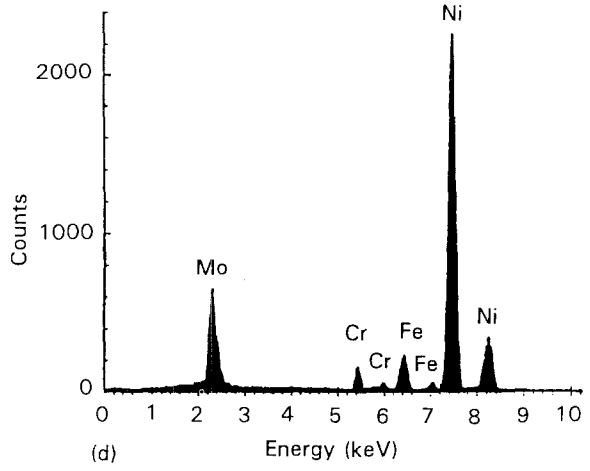

Comparative chemical compositions (wt %)

	Ni_3Mo	Matrix
Ni	57.96	70.32
Mo	33.52	28.32
Fe	5.05	0.87
Cr	3.47	0.49

(e)

Figure 15 Identification of Ni_3Mo in alloy B-2 after 1000 h of ageing at 800 °C (heat B: Ni–28.78Mo–0.98Fe–0.60Cr). (a) Bright-field TEM image illustrating platelets of Ni_3Mo. (b) $[0\,0\,1]_{fcc}$ diffraction pattern of Ni_3Mo. (c) $[1\,1\,1]_{fcc}$ diffraction pattern of Ni_3Mo. (d) X-ray spectrum derived from Ni_3Mo in the STEM mode using a 20-nm probe diameter. (e) Comparative chemical compositions of Ni_3Mo and the matrix solid solution.

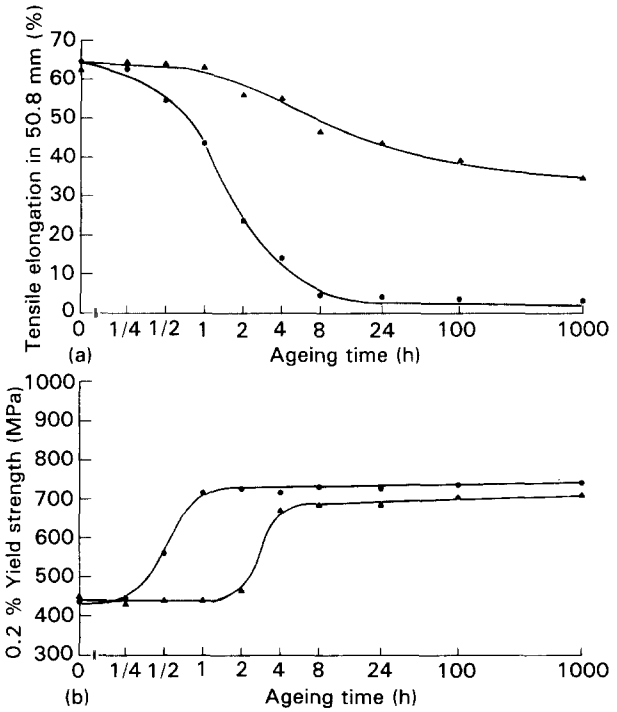

Figure 16 Effect of 5% Cr addition to the Ni–27Mo alloy on its room-temperature tensile properties as functions of ageing time at 700 °C. (a) Elongation; (b) 0.2% yield strength. ●, Ni–27Mo; ▲, Ni–27Mo–5Cr.

exposure, the Ni–27 Mo–5Cr alloy retained about 65% of its initial tensile ductility and maintained a relatively high ductility level after 1000 h of exposure.

Fig. 17 illustrates selected-area electron diffraction patterns derived from the Ni–27 Mo–5Cr alloy in different orientations after 24 h of exposure at 700 °C. In contrast with the Ni–27 Mo alloy where Ni_4Mo was precipitated resulting in superlattice reflections at $1/5\langle 4\,2\,0\rangle$ positions, the only superlattice reflections observed in Fig. 17 are of the type $1/3\langle 4\,2\,0\rangle$ characterizing a Pt_2Mo-type superlattice isomorphous with Ni_2Cr (A_2B-type phase). Based upon the chemical composition of the alloy, it is likely that the composition of the ordered phase was of the type $Ni_2(Cr, Mo)$. Since a Pt_2Mo-type superlattice could form as an intermediate transient phase during Ni_4Mo ordering, it is evident from the above observations that this superlattice was stabilized by the presence of Cr. As illustrated in the dark-field TEM image of Fig. 18a, the A_2B phase assumed the morphology of aligned arrays of discrete particles about 30 to 50 nm in size after 24 h of exposure at 700 °C. With continued ageing up to 1000 h, the ordered phase maintained the same morphology and size as shown in Fig. 18b, an effect similar to the case of Ni_2V [41], and unlike the case of Ni_4Mo described earlier. This result suggested that the strain energy associated with intragranular ordering to the A_2B phase was comparatively smaller in comparison with Ni_4Mo. Another evidence for this difference in behaviour was provided by the absence of a grain boundary ordering reaction in the Ni–27 Mo–5Cr alloy after up to 1000 h of exposure at 700 °C, as shown in Fig. 19. Apparently the grain boundary reaction, which could have an adverse effect on ductility, was suppressed in the Ni–27 Mo–5 Cr alloy due to the comparatively smaller strain energy associated with intragranular ordering to the A_2B phase.

3.6. Effect of Fe on ordering behaviour

Unlike the case of Cr described above, Fe was found to be a stabilizer of only Ni_3Mo. However, the Fe content required to stabilize Ni_3Mo was found to be smaller for a higher Mo content. For example, about 5% Fe was required to completely change the nature of the ordered phase in a Ni–27Mo alloy from Ni_4Mo into Ni_3Mo during ageing at 700 °C. However, about 2% Fe was required to produce a similar result in the stoichiometric Ni–29.1Mo alloy.

Fig. 20 illustrates the effect of Fe additions to the Ni–27Mo alloy on its room-temperature tensile properties as functions of ageing time at 700 °C. Up to about 2% Fe, the only ordered phase identified after 1000 h of exposure was Ni_4Mo. However, in comparison with the Ni–27Mo alloy the ordering kinetics became rather sluggish, suggesting that Fe could reduce the diffusivity of Mo in Ni. When the Fe content was increased to 5%, the ordering kinetics became more sluggish; however, the only ordered phase detected after 1000 h of ageing was found to be Ni_3Mo as illustrated in the example of Fig 21. In the matrix, Ni_3Mo assumed a platelet-type morphology, but at grain boundaries it was in the form of blocky particles.

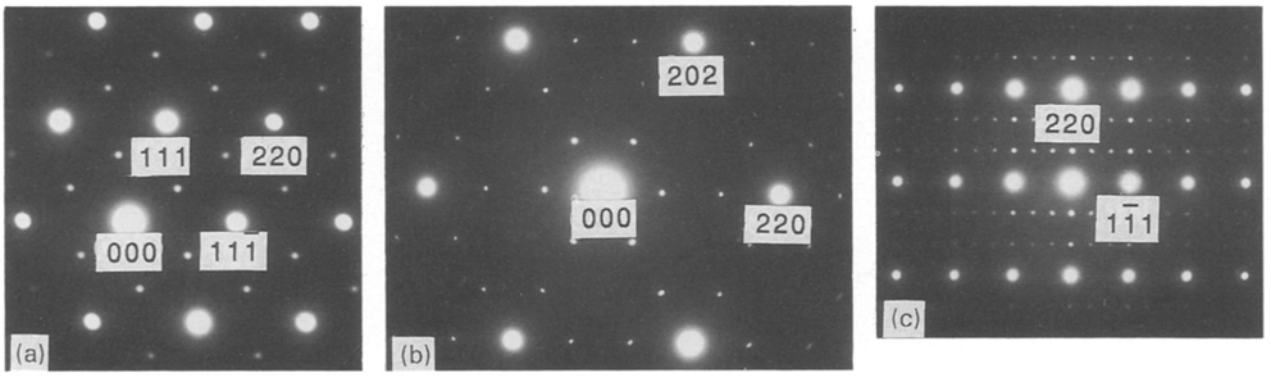

Figure 17 Selected-area diffraction patterns derived from the Ni–27Mo–5Cr alloy after 24 h of ageing at 700 °C; characteristic reflections of the Pt_2Mo-type superlattice are observed at $1/3\langle 4\,2\,0\rangle_{fcc}$ or equivalently at $1/3\langle 2\,2\,0\rangle_{fcc}$ positions. (a) $[1\,\bar{1}\,0]_{fcc}$ orientation; (b) $[1\,\bar{1}\,\bar{1}]_{fcc}$ orientation; (c) $[\bar{1}\,1\,2]_{fcc}$ orientation.

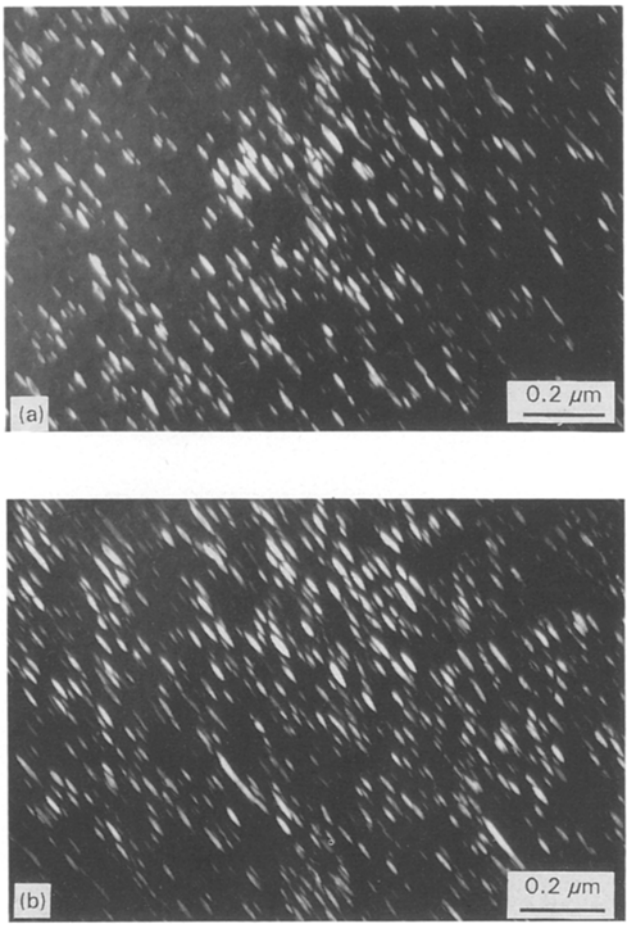

Figure 18 Dark-field TEM images formed with $1/3\langle 4\,2\,0\rangle_{fcc}$ reflections of the Pt_2Mo-type superlattice to illustrate the effect of ageing time at 700° C on the morphology of ordered domains in the Ni–27 Mo–5 Cr alloy. (a) Aged 24 h; (b) Aged 100 h.

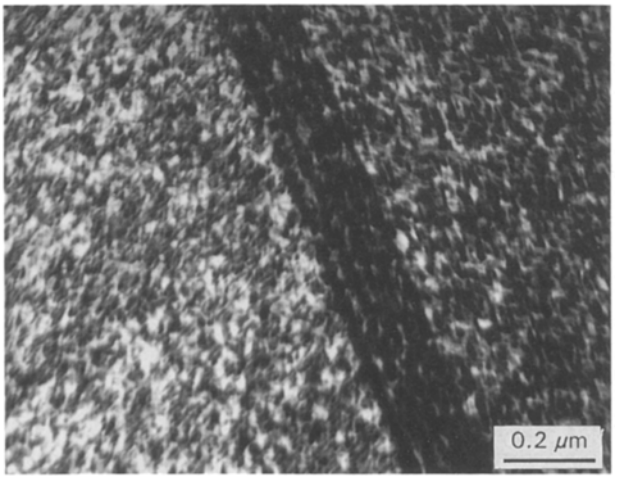

Figure 19 Bright-field TEM image illustrating the absence of discontinuous grain boundary ordering in the Ni–27 Mo–5 Cr alloy after 100 h of ageing at 700 °C.

Relative to the surrounding matrix phase (fcc solid solution), Ni_3Mo was enriched in Fe as demonstrated in the X-ray spectra of Fig. 21, indicating that Fe was an Ni_3Mo stabilizer. In contrast with the case of Cr-containing alloys, all Fe-containing alloys suffered complete loss of ductility during ageing at 700 °C as a result of ordering to either Ni_4Mo and/or Ni_3Mo.

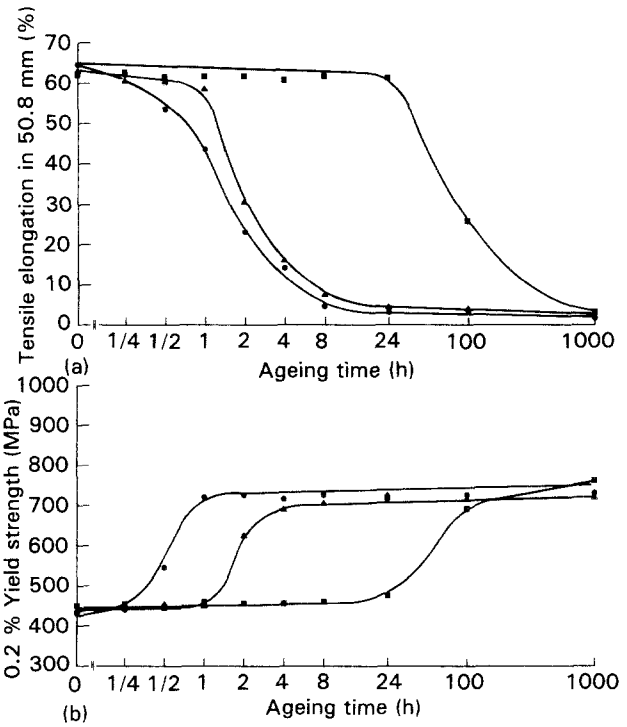

Figure 20 Effect of Fe additions to the Ni–27Mo alloy on the room-temperature tensile properties as functions of ageing time at 700 °C. ●, Ni–27Mo; ▲, Ni–27Mo–2Fe; ■, Ni–27Mo–5Fe.

Combining the above results with those derived from the Cr-containing alloys could further explain the difference in ordering behaviour from one heat to another in the case of alloy B-2. For the typical Cr and Fe concentrations in alloy B-2 (about 2–3%), both elements could act as Ni_3Mo stabilizer in heats containing relatively high Mo content (> 27%) and therefore, the behaviour deviates from that of a binary alloy containing the same Mo concentration. However, for heats containing lower Mo concentrations, the ordered phase becomes Ni_4Mo and the behaviour approaches that of the respective binary alloy as observed.

3.7. Effect of ordering on deformation behaviour

As expected, all alloys studied were found to deform by slip in the disordered state. However, in the ordered state, twinning on $\{1\,1\,1\}_{fcc}$ planes became the predominant deformation mode. Depending upon the state of order including the nature of the ordered phase and its distribution throughout the microstructure, the tensile strain accommodated by twinning varied considerably as demonstrated in the examples given below.

To illustrate the case of Ni_4Mo ordering, Fig. 22 shows the effect of ageing time at 700 °C on the deformation substructure and tensile fracture mode of heat A of alloy B-2 (Table III).

In the disordered state (annealed condition), deformation occurred by slip as shown in Fig. 22a. Slip lines could be clearly distinguished in the deformation substructure with evidence of cross-slip, suggesting a

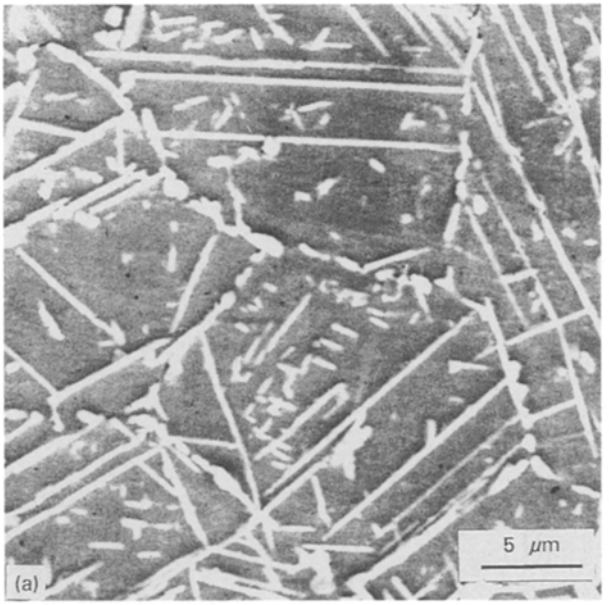

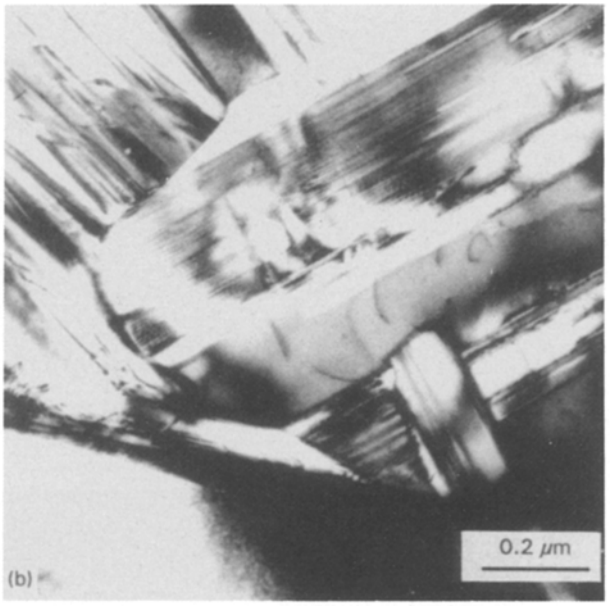

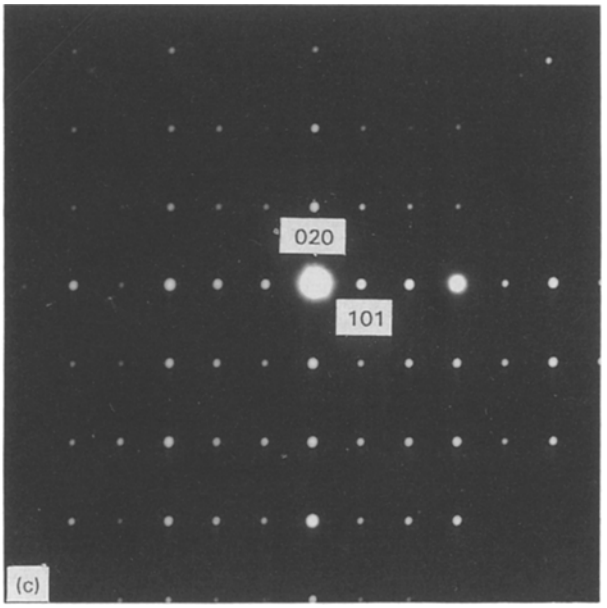

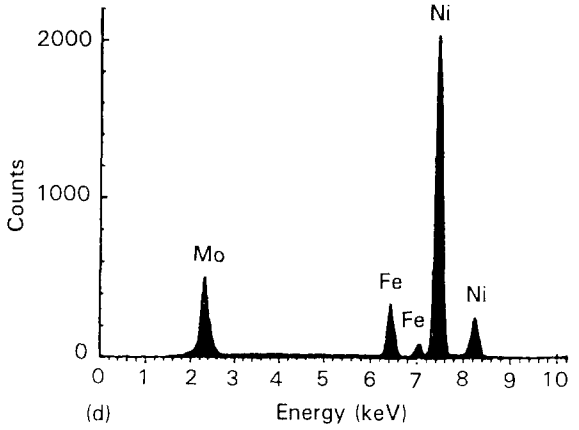

Figure 21 Identification of Ni_3Mo in the Ni–27Mo–5Fe alloy after 1000 h of ageing at 700 °C. (a) Secondary electron SEM image illustrating platelets of Ni_3Mo in the matrix and blocky particles at grain boundaries. (b) Bright-field TEM image of Ni_3Mo platelets. (c) Microdiffraction pattern derived from Ni_3Mo in orthorhombic $[\bar{1}\,0\,1]$ orientation. (d) X-ray spectrum derived from Ni_3Mo in the STEM mode using a 20-nm probe diameter. (e) X-ray spectrum derived from the matrix solid solution in the STEM mode using a 20-nm probe diameter.

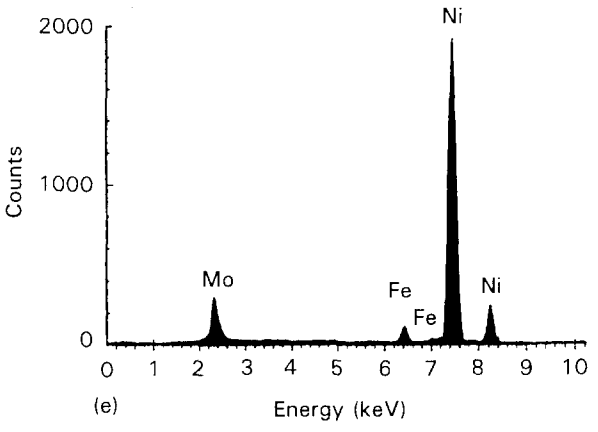

medium stacking fault energy. As expected, the corresponding tensile fracture mode was transgranular (dimple-type rupture).

After ageing for 2 h at 700 °C, and prior to the onset of discontinuous grain boundary precipitation of Ni_4Mo (0.2% yield strength = 710 MPa, tensile ductility = 34%, as shown in Fig. 13), a high density of $\{1\,1\,1\}_{fcc}$ twins was observed in the deformation substructure as shown in Fig. 22b. Deformation by twinning of the $D1_a$ superlattice of Ni_4Mo on $\{1\,1\,1\}_{fcc}$ planes was shown to be energetically more favourable in comparison with deformation by slip [42]. As shown in Fig. 22b, the fracture mode remained transgranular, however the dimples became finer relative to

Figure 22 Bright-field TEM images of substructures (left) and secondary electron SEM images of fracture surfaces (right) illustrating the effect of Ni_4Mo ordering in alloy B-2 on its room-temperature tensile deformation behaviour (heat A: Ni–26.92Mo–0.93Fe–0.64Cr). (a) Annealed (as-quenched); substructure ≡ 6% elongation. (b) Aged 2 h at 700 °C; substructure ≡ 15% elongation. (c) Aged 100 h at 700 °C; substructure ≡ 2% elongation.

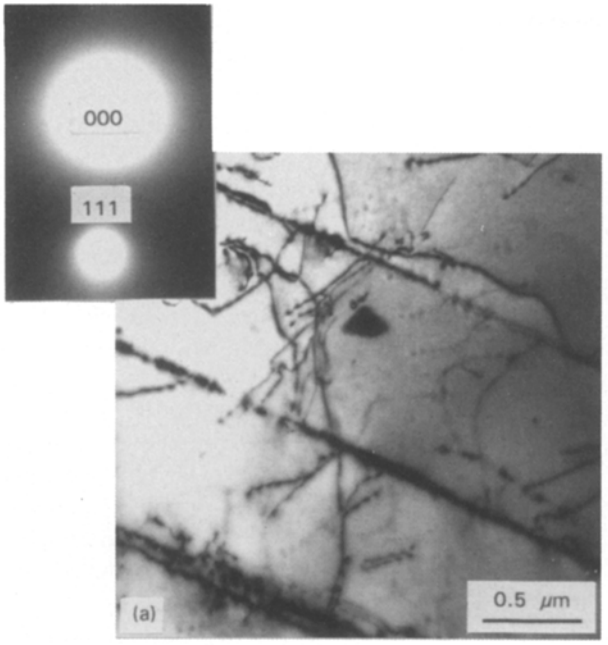
000
111
(a)
0.5 μm

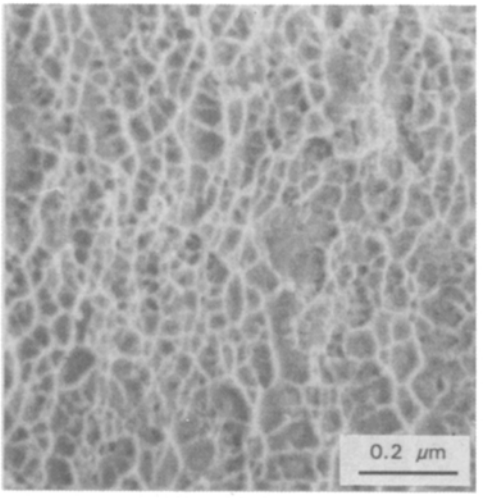
0.2 μm

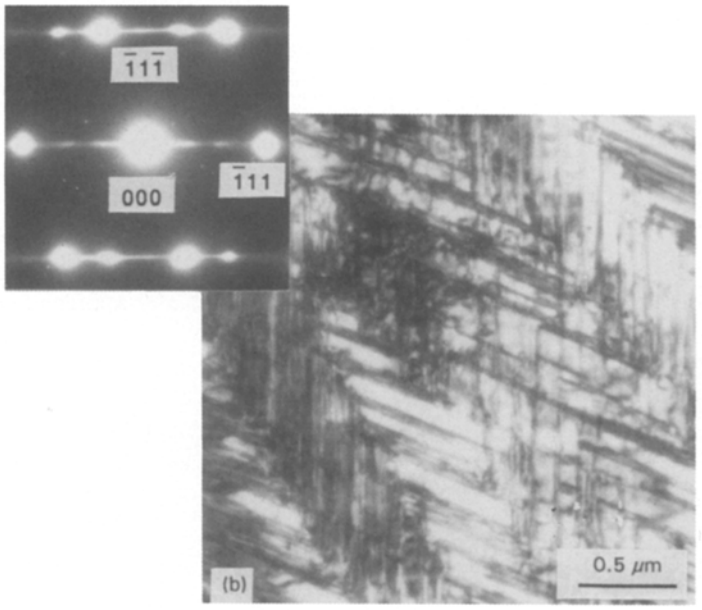
$\bar{1}\bar{1}\bar{1}$
000
$\bar{1}11$
(b)
0.5 μm

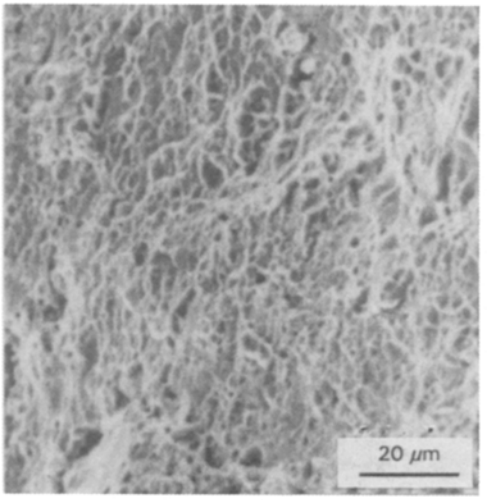
20 μm

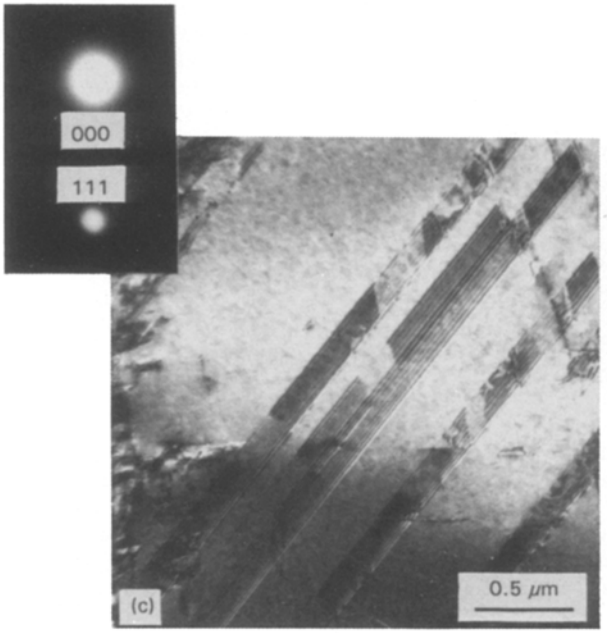
000
111
(c)
0.5 μm

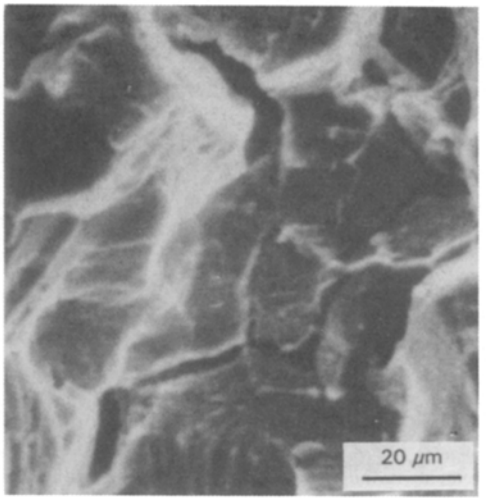
20 μm

the annealed condition, which could be due to nucleation of voids at the Ni_4Mo domains–matrix interface.

As the ageing time was increased to 100 h, the yield strength remained essentially unchanged (715 MPa as shown in Fig. 13), however the tensile ductility was decreased to 3%. At this stage, the deformation substructure contained a high density of $\{1\,1\,1\}_{fcc}$ stacking faults rather than twins as shown in Fig. 22c. Overlapped faults were frequently observed, suggesting a strong tendency towards twinning. Corresponding to this behaviour was the discontinuous grain boundary precipitation of Ni_4Mo, as illustrated in Fig. 11. As seen in Fig. 22c, the fracture mode became predominantly intergranular indicating the embrittlement effect of the grain boundary reaction [4]. Since a $\{1\,1\,1\}_{fcc}$ stacking fault can be envisioned as a very thin layer of a $\{1\,1\,1\}_{fcc}$ twin, it is possible that intergranular fracture occurred before the faults of Fig. 22c could grow into twins.

Similar to the above case, after ordering to the A_2B phase in the Ni–27Mo–5Cr alloy, deformation occurred predominantly by twinning on $\{1\,1\,1\}_{fcc}$ planes as shown in the example of Fig. 23. However, in this case deformation continued to occur by twinning after up to 1000 h of ageing at 700 °C, and the fracture mode remained transgranular as shown in Fig. 23. Also ordered domains were observed in the deformation substructure, as shown in Fig. 23, indicating that deformation of the Pt_2Mo-type superlattice was energetically favourable as reported earlier [43].

Iron-containing alloys ordered to Ni_3Mo exhibited a behaviour somewhat similar to that of alloys ordered to Ni_4Mo, particularly at intermediate stages of ageing where Ni_4Mo and/or a Pt_2Mo-type superlattice were present as intermediate transient phases.

4. Conclusions

Long-range ordering behaviour and the corresponding effects on mechanical properties of selected Ni–Mo-based alloys aged for up to 1000 h at 600–800 °C were studied. All alloys exhibited a similar behaviour during the very early stages of ordering. Initially, the crystallographically-related Pt_2Mo-type, DO_{22} and $D1_a$ superlattices co-existed in the microstructure. As the ordering reaction progressed, however, some of these superlattices became unstable depending upon the exact chemical composition, particularly the Mo, Cr and Fe contents. For alloys of commercial grade containing minor concentrations of Cr and Fe, the ordering behaviour could considerably deviate from that of binary alloys containing the same Mo content. At given Cr and Fe contents, such deviation was found to increase with the Mo content. Depending upon the Mo content, Cr could act as a stabilizer of either Ni_3Mo or a Pt_2Mo-type superlattice isomorphous with Ni_2Cr. Increasing the Mo content was found to promote the role of Cr as Ni_3Mo stabilizer. However, a Pt_2Mo-type superlattice was stabilized at lower Mo contents and at the same Cr level. In contrast, Fe was found to be a stabilizer of only Ni_3Mo depending upon the Mo content. For a given Fe content, the tendency to stabilize Ni_3Mo increased with the Mo content. Although advanced stages of ordering to Ni_4Mo and Ni_3Mo resulted in severe intergranular embrittlement, ordering to a Pt_2Mo-type superlattice in alloys of balanced Mo and Cr contents was found to have beneficial effects on mechanical strength.

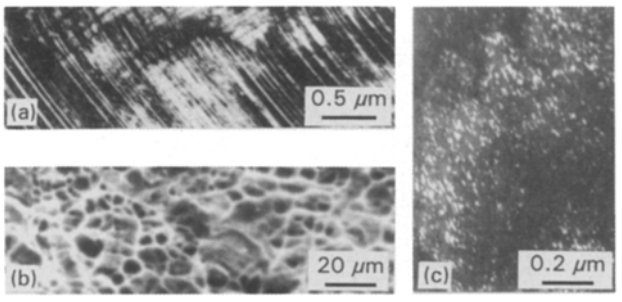

Figure 23 Effect of ordering to a Pt_2Mo-type superlattice in the Ni–27Mo–5Cr alloy on its room-temperature tensile deformation behaviour (aged for 24 h at 700 °C). (a) Bright-field TEM image of the substructure after 15% elongation illustrating $\{1\,1\,1\}_{fcc}$ twins. (b) Secondary electron SEM image of the tensile fracture surface illustrating a transgranular mode. (c) Dark-field TEM image formed with a $1/3\langle 4\,2\,0\rangle_{fcc}$ superlattice reflection to illustrate ordered domains in the deformation substructure.

Acknowledgements

The support of the Research Institute, King Fahd University of Petroleum and Minerals, and permission to publish this work are greatly appreciated.

References

1. F. GALEN HODGE in "Corrosion and corrosion protection handbook" edited by P. A. Schweitzer (Marcel Dekker, New York, 1983) p. 55.
2. W. Z. FRIEND, "Corrosion of nickel and nickel-base alloys" (Wiley, New York, 1980) p. 248.
3. C. R. BROOKS, J. E. SPRUIELL and E. E. STANSBURRY, *Inter. Met. Rev.* **29** (1984) 210.
4. H. M. TAWANCY, *J. Mater. Sci.* **26** (1991) 3955.
5. H. M. TAWANCY and N. M. ABBAS, *ibid.* **24** (1989) 1845.
6. H. M. TAWANCY and A. I. ASPHAHANI in "High-temperature ordered intermetallic alloys" edited by C. C. Koch, C. T. Liu and N. S. Stoloff (Materials Research Society, Pittsburgh, Pennsylvania, vol. **39**, 1984) p. 485.
7. C. R. BROOKS and Y. M. WANG, *Mater. Characterization* **25** (1990) 185.
8. C. R. BROOKS and M. SANGENERIA, *Scripta Met.* **22** (1988) 1683.
9. B. CHAKRAVARTI, E. STRAKE and B. G. LEFEVRE, *J. Mater. Sci.* **5** (1970) 394.
10. H. M. TAWANCY, *Met. Trans.* **22A** (1991) 3067.
11. *Idem, J. Mater. Sci.* **26** (1991) 5933.
12. *Idem, Met. Trans.* **23A** (1992) 1829.
13. M. F. ROTHMAN and H. M. TAWANCY, United States Patent Number 4, 818, 486 (US Patent Office, Washington D. C., April 4, 1989).
14. H. M. TAWANCY, R. B. HERCHENROEDER and A. I. ASPHAHANI, *J. Metals* **35** (1983) 37.
15. H. M. TAWANCY, *J. Mater. Sci.* **16** (1981) 2883.
16. *Idem, Met. Trans.* **11A** (1980) 1764.
17. *Idem, J. Mater. Sci. Lett.* **10** (1991) 696.
18. C. R. BROOKS and Y. M. WANG, *Metallography* **23** (1989) 57.

19. K. VASUDENVAN, PhD thesis, University of Tennessee, Knoxville, Tennessee, 1986.
20. K. VASUDENVAN, MSc thesis, University of Tennessee, Knoxville, Tennessee, 1982.
21. T. S. LEI, PhD thesis, University of Tennessee, Knoxville, Tennessee, 1979.
22. J. P. CHEVALIER and W. STOBBS, *Acta Met.* **27** (1979) 1197.
23. P. R. OKAMOTO and G. THOMAS, *ibid.* **19** (1971) 825.
24. S. C. MOSS and P. C. CLAPP, *Phys. Rev.* **171** (1968) 764.
25. L. E. TANNER and H. J. LEAMY, in "Order-Disorder Transitions in Alloys" edited by H. Warlimont (Springer-Verlag, New York, 1974) p. 180.
26. A. G. KHACHATURYAN, in "Order-Disorder Transitions in Alloys" edited by H. Warlimont (Springer-Verlag, New York, 1974) p. 114.
27. H. M. TAWANCY and M. O. ABOELFOTOH, *Phys. Status Solidi (a)* **99** (1987) 461.
28. H. M. TAWANCY, *Scripta Met.* **18** (1984) 343.
29. G. VAN TENDELOO, *Mater. Sci. Engng* **26** (1976) 209.
30. E. RUEDL, *Mater. Res. Bull.* **10** (1975) 1267.
31. G. VAN TENDELOO, R. DE RIDDER and S. AMELINCKX, *Phys. Status Solidi (a)* **27** (1975) 457.
32. S. M. ALLEN and J. W. CAHN, *Acta Met.* **20** (1972) 423.
33. M. T. RICHARDS and J. W. CAHN, *ibid.* **19** (1971) 1263.
34. L. A. NESBIT and D. E. LAUGHLIN, *ibid.* **26** (1978) 815.
35. W. B. SNYDER and C. R. BROOKS, in "Ordered Alloys: Structural Applications and Physical Metallurgy" edited by B. H. Kear, C. T. Sims, N. S. Stoloff and J. H. Westbrook (Claitor's Publishing Division, Baton Rouge, Louisiana, 1970) p. 275.
36. D. B. WILLIAMS and E. BUTLER, *Int. Met. Rev.* **26** (1981) 153.
37. H. M. TAWANCY, *Mater. Characterization* **28** (1992) 221.
38. H. M. TAWANCY, *J. Mater. Sci. Lett.* **11** (1992) 1446.
39. J. M. OBLAK, D. F. PAULONIS and D. S. DOVAL, *Met. Trans.* **5** (1974) 143.
40. D. B. WILLIAMS and G. CLIFF, in "Principles of Analytical Electron Microscopy", edited by D. C. Joy, A. D. Roming and J. I. Goldstein (Plenum Press, New York, 1986) p. 155. 155.
41. L. E. TANNER, *Acta Met.* **20** (1972) 1197.
42. L. A. NESBIT and D. E. LAUGHLIN, *Acta Met.* **28** (1980) 989.
43. P. D. JOHNSON, PhD thesis, University of Notre Dame, Indiana, 1980.

Received 9 February 1993
and accepted 9 August 1993